Coastal downwelling intensifies landfalling hurricanes

Lewis James Gramer[1,1,1,1], Jun A Zhang[2,2,2,2], Ghassan J. Alaka[3,3,3,3], Andrew Hazelton[4,4,4,4], and Sundararaman Gopalakrishnan[5,5,5,5]

[1]NOAA AOML
[2]Hurricane Research Division, AOML, NOAA
[3]Cooperative Institute for Marine and Atmospheric Studies
[4]University of Miami CIMAS
[5]Hurricane Research Division, AOML,NOAA

November 30, 2022

Abstract

This study demonstrates a link between coastal downwelling and tropical cyclone (TC) intensification. We show coastal downwelling increases air-sea enthalpy (heat, moisture) fluxes ahead of TCs approaching land, creating conditions conducive to intensification even in the presence of typically inhibiting factors like strong vertical wind shear. The study uses a coupled TC model (HWRF-B) and buoy observations to demonstrate that coastal downwelling developed as three TCs in 2020 approached land. Results show downwelling maintained warmer sea-surface temperatures over the ocean shelf, enhancing air-sea temperature/humidity contrasts. We found that in such cases resulting air-sea enthalpy fluxes can replenish the boundary-layer even when cool, dry air intrudes, as in sheared storms and storms approaching continental land-masses. Warm, moist air advects into the inner core, enhancing convective development, thus providing energy for TC intensification. These results indicate coastal downwelling can be important in forecasting TC intensity change before landfall.

Geophysical Research Letters

RESEARCH LETTER
10.1029/2021GL096630

Coastal Downwelling Intensifies Landfalling Hurricanes

Lewis J. Gramer[1,2], Jun A. Zhang[1,2], Ghassan Alaka[2], Andrew Hazelton[1,2], and Sundararaman Gopalakrishnan[2]

[1]Cooperative Institute for Marine and Atmospheric Studies, Miami, FL, USA, [2]NOAA Atlantic Oceanographic and Meteorological Lab, Miami, FL, USA

Key Points:

- Hurricanes approaching land tend to force downwelling over ocean shelves, especially when they move toward or with the coast to their right
- Coastal downwelling sustains warmer shelf sea-surface temperatures (SSTs), even when storm-induced ocean mixing might otherwise cool SSTs
- Sustained shelf SSTs increase heat and moisture fluxes contributing to larger or slower-moving hurricanes' intensification near landfall

Supporting Information:

Supporting Information may be found in the online version of this article.

Correspondence to:

L. J. Gramer,
lew.gramer@noaa.gov

Citation:

Gramer, L. J., Zhang, J. A., Alaka, G., Hazelton, A., & Gopalakrishnan, S. (2022). Coastal downwelling intensifies landfalling hurricanes. *Geophysical Research Letters*, *49*, e2021GL096630. https://doi.org/10.1029/2021GL096630

Received 14 OCT 2021
Accepted 20 APR 2022

Abstract

This study demonstrates a link between coastal downwelling and tropical cyclone (TC) intensification. We show that coastal downwelling increases air-sea enthalpy (heat, moisture) fluxes ahead of TCs as they approach land, creating conditions conducive to intensification even in the presence of typically inhibiting factors like strong vertical wind shear. The study uses a coupled TC model (HWRF-B) and buoy observations to demonstrate that coastal downwelling developed as three TCs in 2020 approached land. Results show downwelling maintained warmer sea-surface temperatures over the ocean shelf, enhancing air-sea temperature/humidity contrasts. We found that in such cases resulting air-sea enthalpy fluxes can replenish the boundary-layer even when cool, dry air intrudes, as in sheared storms and storms approaching continental land-masses. The resulting warm, moist air is advected into the TC inner core, enhancing convective development, thus providing energy for TC intensification. These results indicate coastal downwelling can be important in forecasting TC intensity change before landfall.

Plain Language Summary

We examined forecasts for three hurricanes in 2020 that intensified near landfall. Using a coupled air-sea hurricane model, we found that tropical storm-force winds blowing parallel to the coast forced water near the ocean surface to move toward shore. Winds often blow parallel to the coast when tropical cyclones (TCs) (hurricanes) are near land. The model showed that this movement of water toward shore caused water levels to rise near the coastal boundary - a process called coastal Ekman convergence. This convergence forced water downward along the sloping seafloor and back away from shore, forming a circular exchange of water between the shelf and the open ocean; this exchange is called coastal downwelling. We demonstrate that incipient coastal downwelling brought warmer surface water over the shelf, heating and adding moisture to the air and thus providing more energy to these TCs. We further show that this additional energy provided by coastal downwelling can contribute to intensification of larger or slower-moving TCs before landfall. This result suggests that it is important to validate the modeling of coastal downwelling in future forecast models, in order to reliably forecast TC intensity near landfall.

1. Introduction

In 2009 the National Oceanic and Atmospheric Administration (NOAA) established the 10-year Hurricane Forecast Improvement Program (HFIP; Gopalakrishnan et al., 2021) in part to increase tropical cyclone (TC) forecast accuracy and reliability, especially before landfall. Predicting intensity changes in TCs, particularly rapid intensification (RI; Kaplan et al., 2015), is a complex, multiscale problem. This paper discusses a little-explored mechanism - coastal downwelling - by which some TCs intensify before landfall, even under otherwise unfavorable conditions.

Many studies have shown high sea surface temperatures (SSTs) provide necessary energy for TCs by increasing air-sea enthalpy (heat/moisture) fluxes, resulting in more sustained eyewall convection, warmer cores, lower central pressures, and stronger maximum winds (Emanuel et al., 2004; Jaimes et al., 2015; Zhang, Kalina, et al., 2020; Zhang, Zhang, et al., 2020). Simultaneously, however, stronger near-surface winds impede TC intensification in two ways: frictional dissipation (Wang & Xu, 2010) and SST cooling.

A primary mechanism for SST cooling are cold wakes that TCs can create over the open ocean (e.g., Bender & Ginis, 2000). Such wakes result from entrainment of cooler water into the oceanic mixed layer, and upwelling (rising ocean isotherms) due to divergence of near-surface ocean currents. Resultant SST cooling can significantly weaken TCs (Guo et al., 2020; Walker et al., 2014), particularly slower-moving (e.g., translation speed <2 m/s) and larger ones (radius of maximum winds >50 km; Halliwell et al., 2015).

Several studies of SST change and its influence on TC intensity have also focused on processes over the ocean shelf. Specifically, Glenn et al. (2016) and Seroka et al. (2016) detailed shear-driven vertical ocean-mixing ahead of TC Irene that cooled SSTs over the shelf, inhibiting Irene's intensity. Additionally, coastal downwelling (depression of ocean isotherms), which can sustain SSTs, has been studied by Dzwonkowski et al. (2020) and Miles et al. (2017). Dzwonkowski et al. (2020) observed coastal-ocean warming of ∼2.5°C associated with passage of TC Gordon (2018). Miles et al. (2017) provided dynamical details of coastal downwelling induced by TC Sandy. Studies have also analyzed coastal-ocean processes associated with western Pacific typhoons, for example, Sun et al. (2014), Kuo et al. (2014), and Zhang et al. (2019, 2021).

Environmental vertical wind shear (VWS) in most cases weakens TCs (Wang et al., 2015; Wong & Chan, 2004). This occurs through several processes: vortex-center misalignment (Kaplan et al., 2015), mid-level dry-air intrusion into inner cores (Bhalachandran et al., 2019; Tang & Emanuel, 2010), divergent upper-tropospheric fluxes of entropy and potential energy (Riemer et al., 2010), and downdrafts of cool, dry air into TC boundary layers (e.g., Bhalachandran et al., 2019; Riemer et al., 2010; Tang & Emanuel, 2012). Forecasters typically expect TCs experiencing significant VWS to weaken, particularly those also impacted by ocean cooling.

When approaching landfall, however, TCs sometimes intensify despite ocean mixing, VWS, and the negative effects of land interaction. Hurricane intensification is a multiscale problem which involves nonlinear interactions between ocean and atmosphere. In this study, we establish how three landfalling TCs (Sally, Hanna, and Eta) over the Caribbean Sea and Gulf of Mexico in 2020 intensified before landfall and we highlight the role of coastal downwelling in that intensification. We used the ocean-coupled Basin-scale Hurricane Weather Research and Forecast (HWRF-B) system (Alaka et al., 2020; see also Methods below) together with observations collected from NOAA buoys, to test three hypotheses:

1) TCs approaching land tend to force coastal downwelling over the shelf, especially when the coast lies to their right or ahead of their forward motion.
2) Coastal downwelling can sustain warmer SSTs over the shelf, even when TC-induced ocean vertical mixing and air-sea fluxes might otherwise cool SSTs.
3) Sustained SSTs and resulting air-sea contrasts over the shelf enhance enthalpy fluxes, contributing directly to TC intensification near landfall, particularly for larger or slower-moving TCs.

2. Methods

The model used in this study was Basin-scale HWRF (HWRF-B; Alaka et al., 2017, 2019, 2020; Zhang et al., 2016). HWRF-B uses a fixed single outer domain at 13.5 and telescoping moving nests for each TC at 4.5 and 1.5 km horizontal resolution, but was otherwise configured identically with operational HWRF, including ensemble data-assimilation. HWRF-B is coupled to ocean model Message-Passing Interface Princeton Ocean Model - Tropical Cyclones (MPIPOM-TC; Yablonsky et al., 2015) initialized with a 2-day spinup from the Real-Time Ocean Forecasting System (Mehra & Rivin, 2010). Details of the coupled model configuration together with fuller references are included in the Supporting Information S1. Three case studies from the 2020 Atlantic hurricane season were evaluated: Sally, Hanna, and Eta. Each interacted extensively with the ocean shelf and experienced intensification while approaching landfall. Model fields were analyzed at forecast-hours before and immediately after intensification (Table S1 in Supporting Information S1). We evaluated shelf currents and sea temperatures in MPIPOM-TC using quality-controlled buoy observations from National Oceanic and Atmospheric Administration (NOAA's) National Data Buoy Center (NDBC, 2009; Winant et al., 1994) for TC Sally. Further details of the model and buoy data are provided in Supporting Information S1.

3. Results

Figure 1 shows the effect of downwelling-favorable shelf winds (i.e., local surface winds blowing parallel to and with the coastline on their right) on near-surface ocean currents and sea-surface elevation. Downwelling-favorable winds, which may be common when TCs are near land, force surface Ekman transport toward the lateral boundary of the coast. Over time, this transport results in a sea-surface elevation “bulge” over the shelf due to surface-current convergence. This bulge is the precondition for coastal downwelling.

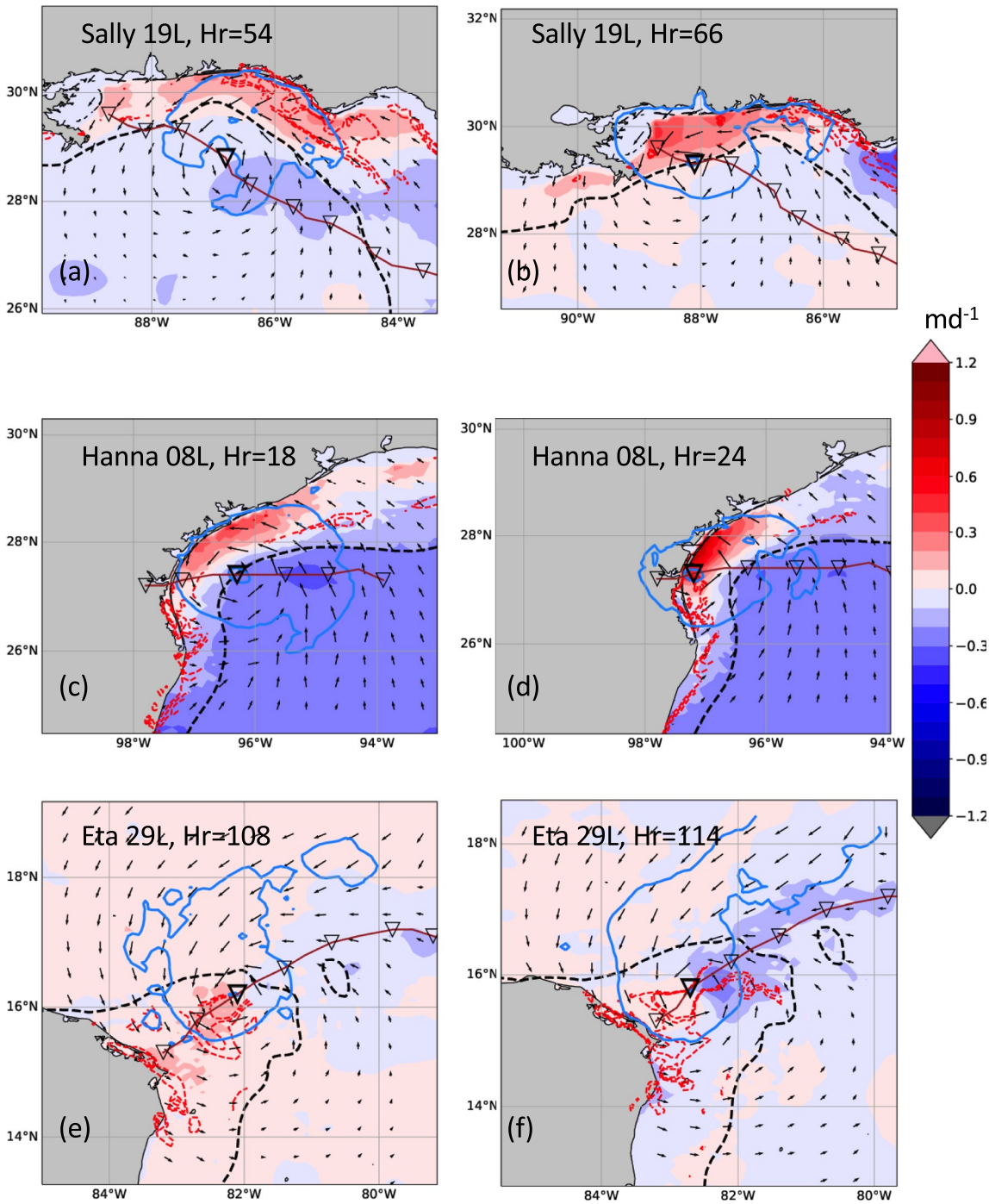

Figure 1. Ocean model fields for tropical cyclones (a and b) Sally, (c and d) Hanna, and (e and f) Eta showing changes in sea-surface elevation (m/day, shading), snapshots of instantaneous surface-current convergence (s^{-1}, dashed red contours), and >17.5 ms^{-1} (>34 kt) surface-wind fields (blue contours). Storm forecast tracks are in brown, triangle markers every 6 hr. Left column shows a forecast hour prior to intensification: (a) hour 54, (c) hour 18, (e) hour 108. Right column shows the forecast hour immediately after intensification: (b) hour 66, (d) hour 24, (f) hour 114.

The left panels in Figure 1 show convergence and the bulge already well-developed before intensification. After intensification (right panels), sea-surface elevation for Sally (Figure 1b) and Hanna (Figure 1d) continued to increase dramatically: As the TCs approached landfall, low sea-level pressure also enhanced storm surge, further increasing elevation. For Eta, wind-speed increase just before landfall was small but surface-current convergence continued to increase through landfall (Figure 1f), consistent with the other cases.

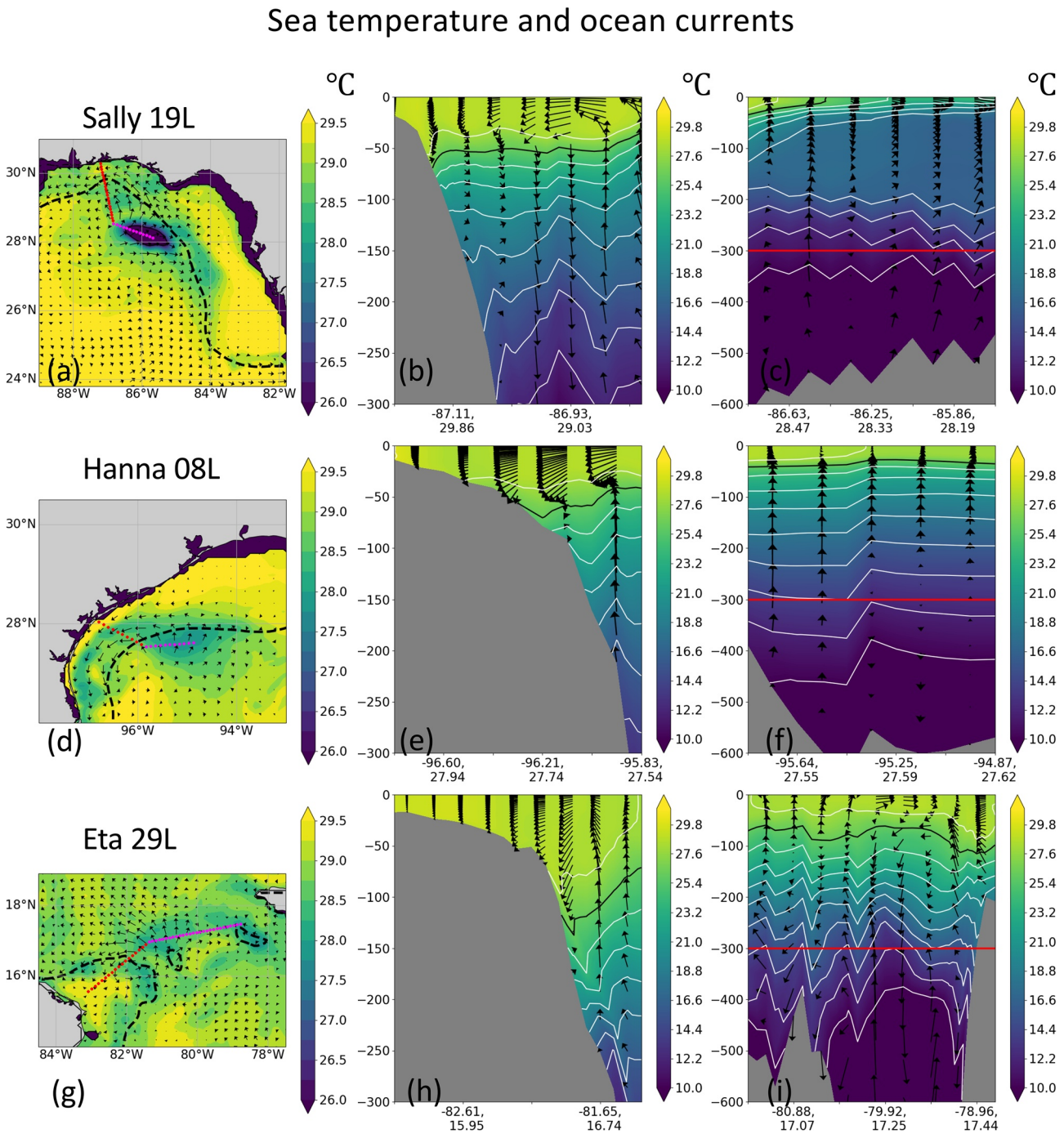

Figure 2. Ocean temperature and currents prior to intensification for: (a–c) Sally, (d–f) Hanna, and (g–i) Eta. Left panels (a, d and g) show sea surface temperature (SST, shading); black dashed contours show 150 m isobaths and black arrows show instantaneous ocean surface currents. Red lines show sections profiled in the middle column; magenta lines show sections profiled in the right column. Middle panels (b, e and h) show cross-sections of sea temperature (shading) and along-track currents (black arrows) over coastal downwelling regions. Right panels (c, f and i) show cross-sections over the upwelling region in each storm's cold-wake (red lines at 300 m highlight cutoff depth of panels in the middle column). White contours in the middle and right columns show sea temperature every 2 K; the contour of the 26°C isotherm is shown in black.

Figure 2 contrasts TC coastal downwelling's effects on sea temperature and ocean currents (left and middle panels) with the effects of the TC wake in the open ocean (right panels): over the shelf, isotherms sloped downward and SSTs were warmer (left and middle columns), consistent with a developing downwelling front. In Sally particularly (Figure 2a), the shelf effect was apparent along the entire west Florida shelf following the storm's

passage. The middle column of Figure 2 shows side views (vertical profiles) of coastal downwelling effects on temperature and ocean currents. Downwelling circulation advected warm water shoreward and then downward, depressing ocean isotherms over the shelf; upward return flows are also apparent offshore. The black contour shows depression of the isotherm for 26°C, a critical temperature threshold for TC intensification (Cione, 2015; Cione & Uhlhorn, 2003). By contrast, side views into each storm's cold wake (right column) show upwelling (due to Ekman divergence) and energetic mixing causing SST cooling.

To evaluate our ocean model's reliability, Figure S1 in Supporting Information S1 compares modeled temperatures and currents with buoy observations from the Gulf of Mexico during Sally's passage. Near-surface sea temperatures from a deep-ocean buoy (Figure S1b in Supporting Information S1) experienced a rapid decline of >1.5°C d^{-1} during TC passage, showing the developing cold wake; however, multiple buoys on the shelf (Figure S1c in Supporting Information S1 shows one example) recorded markedly slower declines of 0.2–0.4°C d^{-1} consistent with SST sustenance from downwelling. Figures S1d and S1e in Supporting Information S1 show a close correspondence between near-surface currents in the forecast and available buoy current-profiler observations on the west Florida shelf.

Figure S2 in Supporting Information S1 demonstrates the persistence of downwelling-favorable winds over the shelf for each case. Shading in the right-hand panels shows the length of time, divided by the local inertial period, when alongshore winds of >5 kts were blowing with the coast on their right: downwelling-favorable winds blew over the shelf for from one to three times the local inertial period in each case, consistent with the full development of downwelling as described in Austin and Lentz (2002). Additional profile snapshots in Figure S3 of Supporting Information S1 show development of convergence and the resulting downwelling (isotherm depression) on the shelf. Figure S4 and Figure S5 in Supporting Information S1 are depth-vs.-time Hovmöller diagrams at points on the outer shelf near the center of each region of sustained SST. Together they show that vertical ocean mixing tended to smooth vertical gradients in near-surface temperature and salinity, particularly as each TC approached nearest that point. However, these figures also show that, prior to each TC's approach, downwelling-driven isotherm depression and cross-shelf lateral heat-transport created conditions such that vertical mixing resulted in very little surface cooling. Figure S6 in Supporting Information S1 shows lower-salinity water near the surface for each case. Figures S5a and S6a in Supporting Information S1 show that a low-salinity lens likely inhibited vertical mixing in Sally, although it may also have allowed downwelling to extend shoreward (Csanady, 1982; Lentz, 2001). However, for Hanna and Eta, the figures show that the locations of low-salinity lenses did not coincide with the regions of highest sustained SST (e.g., Figure 2) and enhanced air-sea enthalpy flux (Figure 3); thus, barrier layers (Rudzin et al., 2020) probably did not play a role in these two cases.

Figure 3 shows positive total (latent+sensible) air-sea enthalpy fluxes over the shelf, which potentially aided intensification of each TC despite moderate-to-strong deep-layer (200–850 hPa; Table S1 in Supporting Information S1) VWS and surface wind-field asymmetries. The enthalpy fluxes prior to intensification (left panels) were more prominent over the shelf than over deeper water. Peak enthalpy fluxes per grid-point for Sally, Hanna, and Eta were 1,128, 1,223, and 1,570 Wm^{-2}, respectively; all these peaks occurred over the ocean shelf.

The enhanced shelf fluxes illustrated coastal downwelling's impact on air-sea temperature and humidity contrasts before intensification. For although asymmetries were apparent in both enthalpy fluxes and surface-wind fields, areas of enhanced enthalpy flux in all panels corresponded with areas of large air-sea humidity and temperature contrasts over the shelf, and not always with areas of the strongest surface winds (not shown). Thus, shelf-based enthalpy fluxes resulted from higher SSTs over the shelf rather than simple wind asymmetries. These asymmetric fluxes counterintuitively led to a more symmetrized TC after intensification (Figure 3 and Figure 4 right panels).

Figure 4 shows cool, dry air of low equivalent potential temperature (θ_e) carried by downdrafts and coastal winds into the boundary layer of each storm. Enthalpy fluxes over the shelf (Figure 3) replenished boundary-layer heat and moisture; this increased θ_e in the 6–12 hr between the left and right panels of Figure 4, even for more strongly sheared storms Sally and Eta. During intensification, surface air flow along the streamlines shown in Figure 4 transported higher-θ_e air into the inner core of each storm, enhancing mid-level and deep convection and resulting in symmetrization and intensification just before landfall (right panels).

Figures 3 and 4 show that axisymmetrization and contraction preceded TC intensification, consistent with Chen et al. (2018) and Wadler et al. (2021). Advection of entropy-replenished boundary-layer air into the inner core enhanced eyewall convection and drove diabatic heating, which is favorable for symmetric intensification of

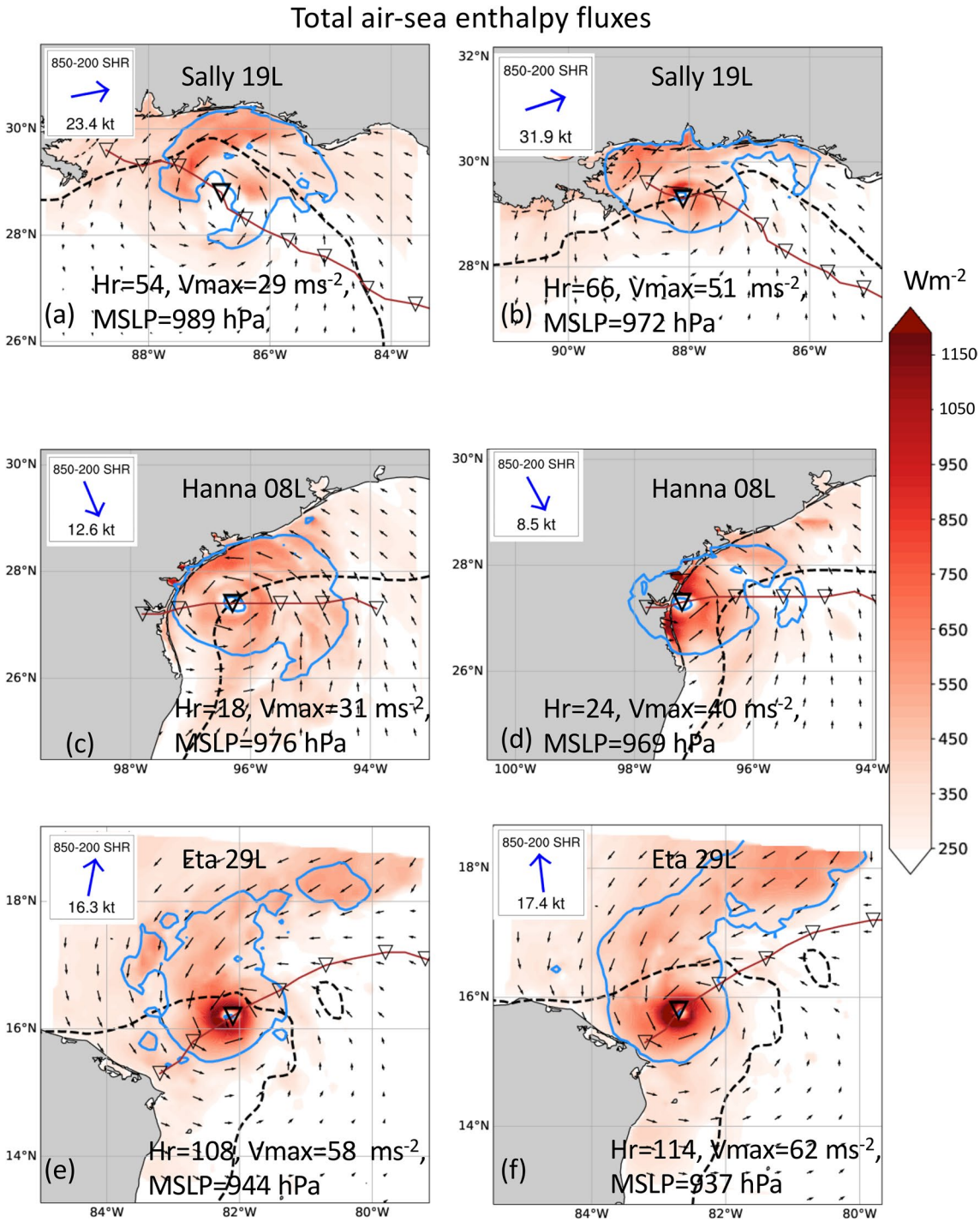

Figure 3. Total air-sea enthalpy fluxes (W/m^2, shading), with snapshots of instantaneous >17.5 ms^{-1} surface wind field (blue contours) and wind direction (black arrows), 150 m isobath (black dashed line), and forecast tropical cyclone track (brown lines,triangles), for: (a–b) Sally, (c–d) Hanna, and (e–f) Eta. Forecast-hours are as in Figure 1. Insets indicate vertical wind shear (VWS) between 850 and 200 hPa, maximum 10 m wind speed [ms^{-1}] (V_{max}), and minimum sea-level pressure [hPa] (MSLP) at the forecast-hour shown.

the TC vortex (Chen et al., 2018), especially when located inside the radius of maximum winds (e.g., Chen and Gopalakrishnan, 2015; Vigh & Schubert, 2009). But all three TCs moved relatively slowly (Table S1 in Supporting Information S1), which would have been expected both to increase the effect of the cold wake on fluxes over deeper water and to allow VWS to exacerbate initial asymmetries, weakening these TCs. The subsequent intensification of each storm, despite these effects, was remarkable and largely attributable to the shelf effect.

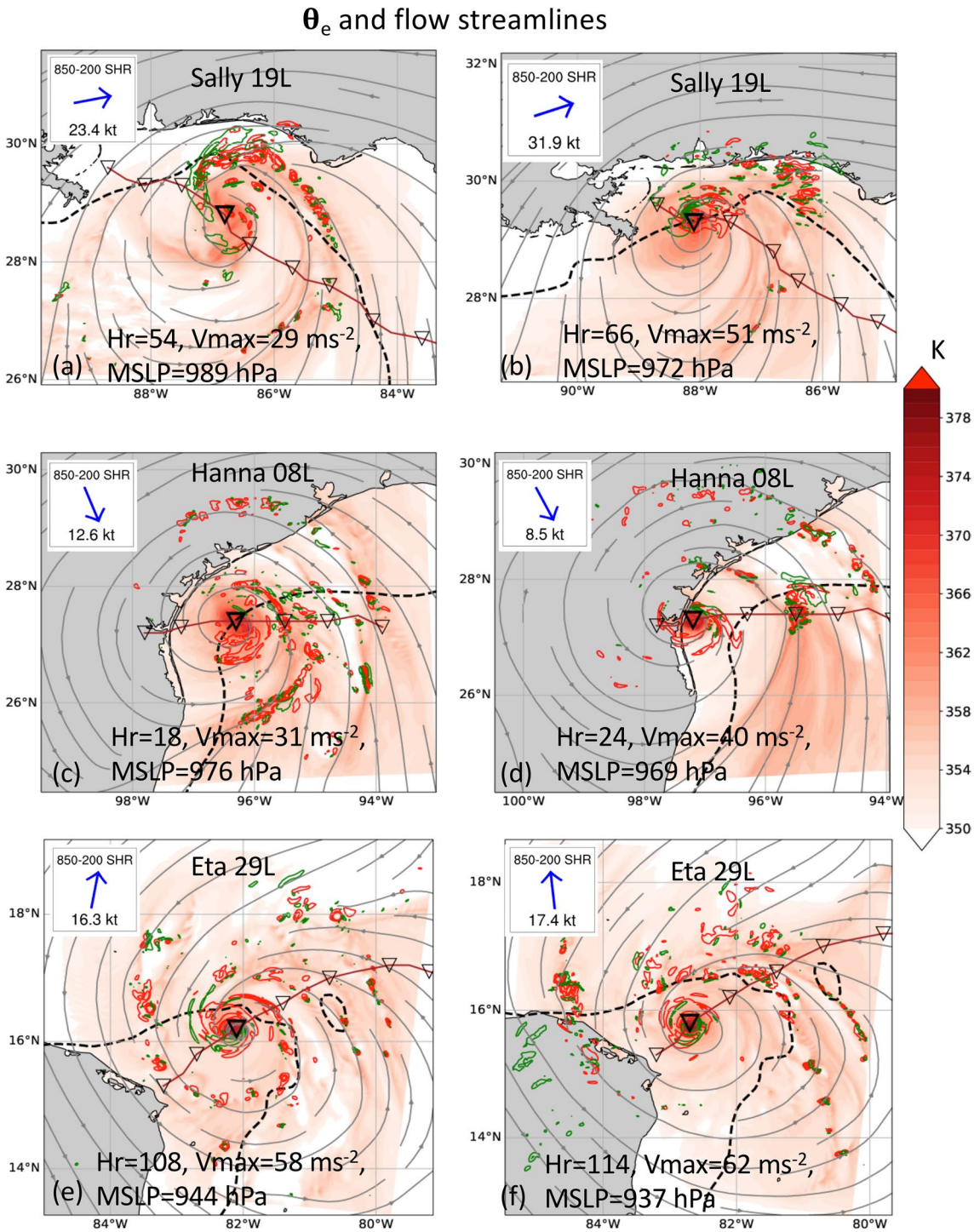

Figure 4. Mean equivalent potential temperature (θ_e,shading), vertical velocity (contours) and mean wind streamlines below 850 hPa (gray). Green contours denote downdrafts ($w < -0.75$ ms^{-1} below 600 hPa); red contours denote updrafts ($w > 2.0$ ms^{-1} above 600 hPa). Forecast-hours are as in Figure 1. Insets show vertical wind shear, V_{max}, and minimum sea-level pressure (MSLP) as in Figure 3.

In Figure 5, we evaluate the simplified energy budget terms (Equation S1 in Supporting Information S1). Change in total kinetic energy and in maximum 10 m winds for all three storms positively correlated with the difference between total enthalpy fluxes and frictional dissipation. Enthalpy fluxes over the shelf region constituted an important fraction of the total fluxes (30%–90%) leading up to and during intensification. Increases in kinetic

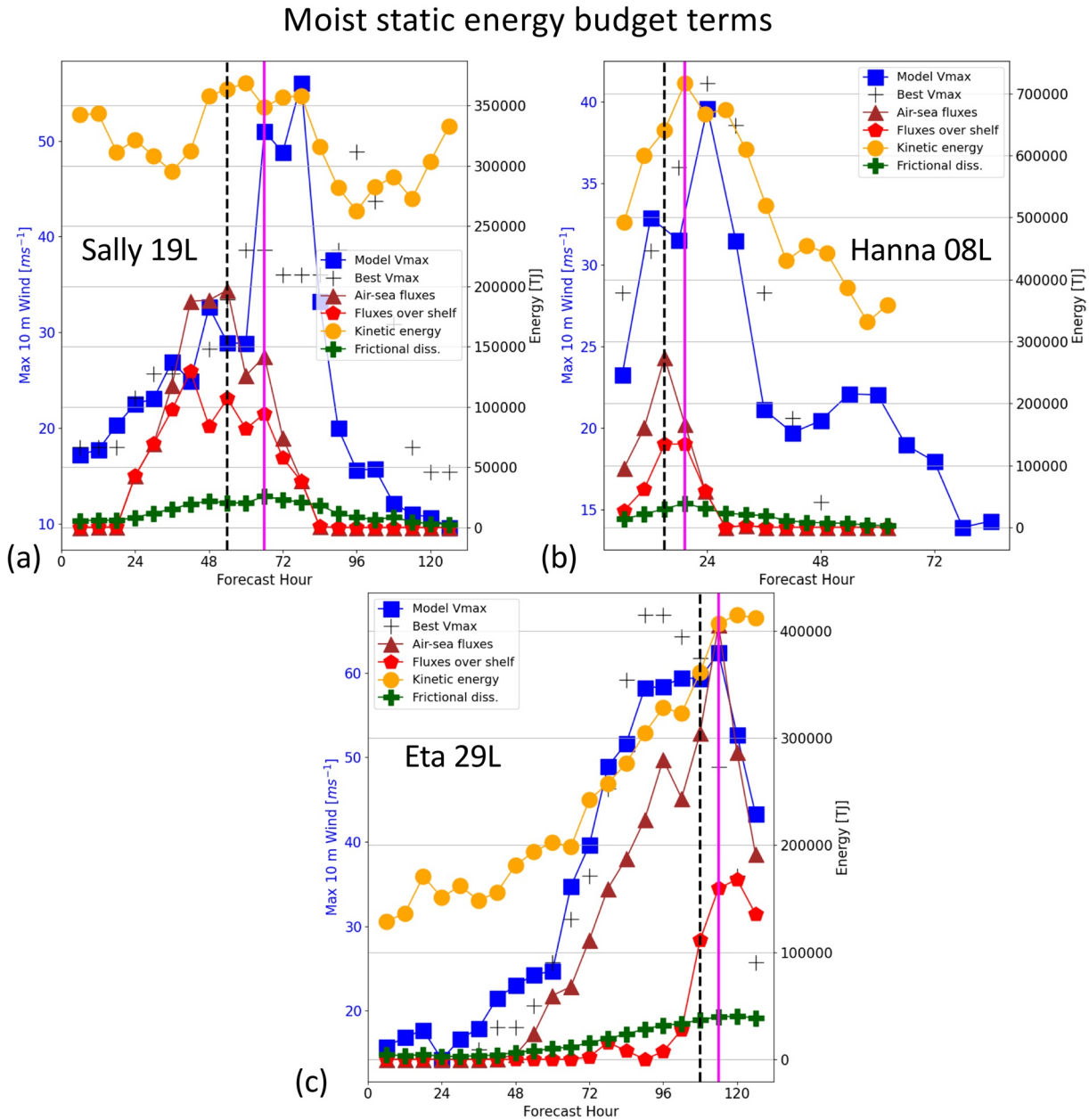

Figure 5. Simplified energy budget terms (from Equation S1 in Supporting Information S1) in terajoules (scale in black axis at right of each panel), including: total air-sea enthalpy flux ($THF_d + THF_s$, brown lines, triangles), enthalpy flux over the shelf only (THF_s, red lines, pentagons), frictional dissipation (FD, green lines and green "+"), and total kinetic energy (KE, orange lines, circles). Maximum 10 m wind speed in ms^{-1} is shown in blue (axis at left, blue line, square markers), along with best-track maximum speed (black "+"). Panels show: (a) Sally, (b) Hanna, and (c) Eta. Note differing vertical scales between panels.

energy lagged increases in surface fluxes by 6–12 hr, suggesting that surface enthalpy fluxes lead to TC intensity change.

Peaks in total enthalpy flux preceded an intensification of 15 ms^{-1} in 36 hr for Sally (Figure 5a) and the RI (Kaplan & DeMaria, 2003) of 16 ms^{-1} in 18 hr for Hanna (Figure 5b); the shelf effect contributed a majority of the total flux in both cases. Although Eta intensified largely over the open ocean, it encountered insular and continental shelf water starting in hour 72, deriving 30%–40% of its flux from the shelf as it approached maximum forecast intensity near landfall (Figure 5c). These shelf fluxes occurred in both the inner and outer core of Eta (Figure 3e). High enthalpy fluxes in all three cases supported boundary-layer recovery of downdraft-induced and continental low-entropy air upshear, before that air entered updrafts in the downshear quadrant (Figure 4),

leading to TC intensification. This process thus countered the negative effects of shear and ventilation on intensity (Figure 5).

4. Discussion and Conclusions

This paper investigated coastal downwelling in three hurricane case-studies using the coupled HWRF-B/MPIPOM-TC modeling system. Coastal downwelling develops when surface winds blow with the land to their right in the Northern Hemisphere for a sufficient period (Austin & Lentz, 2002; Kuo et al., 2014; Shen et al., 2017; Sreenivas & Gnanaseelan, 2014; Zhang et al., 2019). We found that downwelling-favorable winds, blowing for more than one local inertial period, forced coastal downwelling ahead of each TC. We further found that the coastal downwelling associated with each TC sustained SSTs over the shelf, consistent with other studies focused on non-TC conditions (e.g., Choboter et al., 2011). Shelf circulation during typhoons in the western north Pacific has been observed to sustain SSTs (Kuo et al., 2014; Zhang et al., 2019, 2021), while coastal downwelling in particular has been implicated in TC intensification by some studies of Atlantic hurricanes (Dzwonkowski et al., 2020; Miles et al., 2017).

Our results contrast with those of previous studies, including Glenn et al. (2016), which showed cooling over the Mid-Atlantic Bight during passage of Hurricane Irene (2011). In that and some other cases reviewed by Glenn et al., near-bottom regions on the shelf harbored pools of cooler water before storm passage, and TCs approached with the coast on their left. In our case studies, water near the shelf-floor prior to storm passage was generally above 26°C out to the 50 m isobath (Figure 2, Figure S2 in Supporting Information S1), and each TC approached the shelf with land on its right or ahead of it. Our analysis thus suggests that, for a number of cases in 2020, shear-driven vertical mixing could not compensate for coastal downwelling's effects.

We established a direct link between SST sustenance, enhanced enthalpy fluxes, and intensification for these three Atlantic TCs. Despite dry-air intrusion due to persistent shear, enhanced air-sea enthalpy fluxes resulting from warmer SSTs over the shelf caused the TCs to intensify before landfall. Surface wind-field forecasts and observations (figures omitted) showed warmer, moister air in the boundary layers being carried into the inner cores over a period of 6–12 hr; increases in both total kinetic energy and surface winds followed within another 6–12 hr. A detailed understanding of the vortex spin-up process under these conditions will be carried out in a later work.

A simplified moist static energy budget showed that peaks in the residual of air-sea enthalpy flux minus frictional dissipation correlated with maximum TC intensity, similar to results for peak intensity found by Wang and Xu (2010). The lag of 12–18 hr between peak air-sea enthalpy flux and maximum TC intensity was consistent with idealized air-sea modeling studies (Halliwell et al., 2015). Our results support the conclusion that surface enthalpy fluxes are important for TC intensity change, constituting an energy source sufficient to compensate for energy loss due to frictional dissipation (Emanuel, 1986). Similarly, we find agreement with Zhang et al. (2017) that the influence of surface enthalpy fluxes for TC intensification hinges on their role in boundary-layer recovery. The novel result here is the importance of air-sea enthalpy fluxes due particularly to TC-driven coastal downwelling.

Future work will examine the relationship between shelf-fluxes and storm structure (wind-field sizes), which are important in forecasting TC hazards and may also constitute an important component of TC response to the shelf effect. Future work will also examine boundary-layer recovery mechanisms within the TC core, potentially using idealized studies. Finally, a recent study suggests insolation differences related to cloud-cover may be important for TC intensification near landfall (Lok et al., 2021): we will extend the energy budget discussed here (Equation S1 in Supporting Information S1) to consider radiative fluxes in addition to terms for potential- and internal-energy advection.

This study demonstrated that the coupled HWRF-B/MPIPOM-TC system appropriately modeled important coastal- and shelf-ocean dynamics related to TC intensification, namely the shelf effect due to coastal downwelling. We further showed this oceanographic process can impact boundary-layer recovery, atmospheric convection, and TC intensity. Three TCs from just one basin and hurricane season (2020 North Atlantic) were impacted by coastal downwelling; other cases from the 2017–2020 North Atlantic and eastern North Pacific hurricane

seasons are being analyzed to determine the relative prevalence of this shelf effect in causing intensification of landfalling TCs.

Future model-observational studies should analyze other oceanographic mechanisms that may contribute to the shelf effect, including barrier-layer intensification (Balaguru et al., 2020; Rudzin et al., 2020) as well as ocean internal, coastal-trapped, and continental shelf waves (Shen et al., 2021). Examining implications of the shelf effect for TCs in a changing climate is also important (Emanuel, 2017). Finally, future work must evaluate how the shelf effect can impact coastal communities and marine ecosystems, for example, from enhanced bottom temperatures and cross-shore transports (Dzwonkowski et al., 2020).

Above all, this study establishes the importance of coastal downwelling in increasing storm intensity before landfall. To ensure reliable intensity forecasts for landfalling TCs, we recommend modeling of the shelf effect be validated in future upgrades of operational coupled TC forecast models, such as the Hurricane Analysis and Forecast System (HAFS; Hazelton et al., 2022) now under development by HFIP (Gall et al., 2013).

Data Availability Statement

The numerical model simulations upon which this study is based are available via public FTP at https://storm.aoml.noaa.gov/users/lgramer/Gramer_2022_1_data.tgz. In addition, HWRF is a community model with a code repository that is publicly available at https://dtcenter.org/community-code/hurricane-wrf-hwrf/download. The HWRF-B code repository is located at https://svn-dtc-hwrf.cgd.ucar.edu/branches/HB20 and can be shared with interested parties upon request along with all information required to replicate the simulations. Graphical products associated with TC forecasts described in this text can be found online at https://storm.aoml.noaa.gov.

Acknowledgments
The authors wish to thank the Hurricane Forecast Improvement Program (HFIP) as well as funding from the Hurricane Supplemental (HSUO), National Oceanic and Atmospheric Administration (NOAA) Grant NA19OAR0220187, NOAA Grant NA19OAR0220187, and ONR Grant N00014-20-6891-2071. We are also grateful for the insightful questions and comments from two anonymous reviewers, which led to significant improvements in the work. Internal review comments from F Marks, R Rogers, and R Lumpkin all improved the manuscript. LJG is particularly thankful to lively recent discussions with H-S Kim, and earlier discussions with SJ Monismith and P Graves. Finally, suggestions from E Becker, L Albritton, K Nielsen, A Mann, A Sanchez-Garcia, and N Deyo of the University of Miami all improved the clarity and concision of the manuscript.

References

Alaka, G. J., Jr., Zhang, X., Gopalakrishnan, S. G., Goldenberg, S. B., & Marks, F. D. (2017). Performance of basin-scale HWRF tropical cyclone track forecasts. *Weather and Forecasting*, *32*(3), 1253–1271. https://doi.org/10.1175/WAF-D-16-0150.1

Alaka, G. J., Jr., Zhang, X., Gopalakrishnan, S. G., Zhang, Z., Marks, F. D., & Atlas, R. (2019). Track uncertainty in high-resolution HWRF ensemble forecasts of Hurricane Joaquin. *Weather and Forecasting*, *34*(6), 1889–1908. https://doi.org/10.1175/WAF-D-19-0028.1

Alaka, G. J., Sheinin, D., Thomas, B., Gramer, L., Zhang, Z., Liu, B., et al. (2020). A hydrodynamical atmosphere/ocean coupled modeling system for multiple tropical cyclones. *Atmosphere*, *11*(8), 869. https://doi.org/10.3390/atmos11080869

Austin, J. A., & Lentz, S. J. (2002). The inner shelf response to wind-driven upwelling and downwelling. *Journal of Physical Oceanography*, *32*(7), 2171–2193. https://doi.org/10.1175/1520-0485(2002)032<2171:tisrtw>2.0.co;2

Balaguru, K., Foltz, G. R., Leung, L. R., Kaplan, J., Xu, W. W., Reul, N., & Chapron, B. (2020). Pronounced impact of salinity on rapidly intensifying tropical cyclones. *Bulletin of the American Meteorological Society*, *101*(9), E1497–E1511. https://doi.org/10.1175/bams-d-19-0303.1

Bender, M. A., & Ginis, I. (2000). Real-case simulations of hurricane-ocean interaction using a high-resolution coupled model: Effects on hurricane intensity. *Monthly Weather Review*, *128*(4), 917–946. https://doi.org/10.1175/1520-0493(2000)128<0917:rcsoho>2.0.co;2

Bhalachandran, S., Haddad, Z. S., Hristova-Veleva, S. M., & Marks, F. D. (2019). The Relative importance of factors influencing tropical cyclone rapid intensity changes. *Geophysical Research Letters*, *46*(4), 2282–2292. https://doi.org/10.1029/2018gl079997

Chen, H., & Gopalakrishnan, S. G. (2015). A study on the asymmetric rapid intensification of Hurricane Earl (2010) using the HWRF system. *Journal of the Atmospheric Sciences*, *72*(2), 531–550. https://doi.org/10.1175/jas-d-14-0097.1

Chen, X. M., Xue, M., & Fang, J. (2018). Rapid intensification of typhoon mujigae (2015) under different sea surface temperatures: Structural changes leading to rapid intensification. *Journal of the Atmospheric Sciences*, *75*(12), 4313–4335. https://doi.org/10.1175/jas-d-18-0017.1

Choboter, P. F., Duke, D., Horton, J. P., & Sinz, P. (2011). Exact solutions of wind-driven coastal upwelling and downwelling over sloping topography. *Journal of Physical Oceanography*, *41*(7), 1277–1296. https://doi.org/10.1175/2011jpo4527.1

Cione, J. J. (2015). The relative roles of the ocean and atmosphere as revealed by buoy air-sea observations in hurricanes. *Monthly Weather Review*, *143*(3), 904–913. https://doi.org/10.1175/mwr-d-13-00380.1

Cione, J. J., & Uhlhorn, E. W. (2003). Sea surface temperature variability in hurricanes: Implications with respect to intensity change. *Monthly Weather Review*, *131*(8), 1783–1796. https://doi.org/10.1175//2562.1

Csanady, G. T. (1982). *Circulation in the coastal ocean* (p. 279). D. Reidel Pub. Co.

Dzwonkowski, B., Coogan, J., Fournier, S., Lockridge, G., Park, K., & Lee, T. (2020). Compounding impact of severe weather events fuels marine heatwave in the coastal ocean. *Nature Communications*, *11*(1), 1–10. https://doi.org/10.1038/s41467-020-18339-2

Emanuel, K. (2017). Will global warming make hurricane forecasting more difficult? *Bulletin of the American Meteorological Society*, *98*(3), 495–501. https://doi.org/10.1175/bams-d-16-0134.1

Emanuel, K., DesAutels, C., Holloway, C., & Korty, R. (2004). Environmental control of tropical cyclone intensity. *Journal of the Atmospheric Sciences*, *61*(7), 843–858. https://doi.org/10.1175/1520-0469(2004)061<0843:ecotci>2.0.co;2

Emanuel, K. A. (1986). An air sea interaction theory for tropical cyclones .1. Steady-state maintenance. *Journal of the Atmospheric Sciences*, *43*(6), 585–604. https://doi.org/10.1175/1520-0469(1986)043<0585:aasitf>2.0.co;2

Gall, R., Franklin, J., Marks, F., Rappaport, E. N., & Toepfer, F. (2013). The Hurricane Forecast Improvement Project. *Bulletin of the American Meteorological Society*, *94*(3), 329–343. https://doi.org/10.1175/bams-d-12-00071.1

Glenn, S. M., Miles, T. N., Seroka, G. N., Xu, Y., Forney, R. K., Yu, F., et al. (2016). Stratified coastal ocean interactions with tropical cyclones. *Nature Communications*, *7*(10887), 1–10. https://doi.org/10.1038/ncomms10887

Gopalakrishnan, S., Toepfer, F., Forsythe-Newell, S., Gall, R., Marks, F., Rappaport, E. N., et al. (2021). *HFIP R&D activities summary: Recent results and operational implementation* (p. 2020). HFIP Technical Report: HFIP2021-1 Retrieved from https://hfip.org/sites/default/files/documents/hfip-annual-report-2020-final_0.pdf

Guo, T., Sun, Y., Liu, L., & Zhong, Z. (2020). The impact of storm-induced SST cooling on storm size and destructiveness: Results from atmosphere-ocean coupled simulations. *Journal of Meteorological Research*, *34*(5), 1068–1081. https://doi.org/10.1007/s13351-020-0001-2

Halliwell, G. R., Gopalakrishnan, S., Marks, F., & Willey, D. (2015). Idealized study of ocean impacts on tropical cyclone intensity forecasts. *Monthly Weather Review*, *143*(4), 1142–1165. https://doi.org/10.1175/mwr-d-14-00022.1

Hazelton, A., Gao, K., Bender, M., Cowan, L., Alaka, G. J., Jr., Kaltenbaugh, A., et al. (2022). Performance of 2020 Real-Time Atlantic Hurricane Forecasts from High-Resolution Global-Nested Hurricane Models: HAFS-globalnest and GFDL T-SHiELD. *Weather and Forecasting*, *37*(1), 143–161. https://doi.org/10.1175/WAF-D-21-0102.1

Jaimes, B., Shay, L. K., & Uhlhorn, E. W. (2015). Enthalpy and momentum fluxes during Hurricane Earl relative to underlying ocean features. *Monthly Weather Review*, *143*(1), 111–131. https://doi.org/10.1175/mwr-d-13-00277.1

Kaplan, J., & DeMaria, M. (2003). Large-scale characteristics of rapidly intensifying tropical cyclones in the North Atlantic basin. *Weather and Forecasting*, *18*(6), 1093–1108. https://doi.org/10.1175/1520-0434(2003)018<1093:lcorit>2.0.co;2

Kaplan, J., Rozoff, C. M., DeMaria, M., Sampson, C. R., Kossin, J. P., Velden, C. S., et al. (2015). Evaluating environmental impacts on tropical cyclone rapid intensification predictability utilizing statistical models. *Weather and Forecasting*, *30*(5), 1374–1396. https://doi.org/10.1175/waf-d-15-0032.1

Kuo, Y. C., Lee, M. A., & Chern, C. S. (2014). Typhoon-induced ocean responses off the southwest coast of Taiwan. *Ocean Dynamics*, *64*(11), 1569–1581. https://doi.org/10.1007/s10236-014-0776-8

Lentz, S. J. (2001). The influence of stratification on the wind-driven cross-shelf circulation over the North Carolina shelf. *Journal of Physical Oceanography*, *31*(9), 2749–2760. https://doi.org/10.1175/1520-0485(2001)031<2749:tiosot>2.0.co;2

Lok, C. C., Chan, J. C., & Toumi, R. (2021). Tropical cyclones near landfall can induce their own intensification through feedbacks on radiative forcing. *Communications Earth & Environment*, *2*(1), 1–10. https://doi.org/10.1038/s43247-021-00259-8

Mehra, A., & Rivin, I. (2010). A Real Time Ocean Forecast System for the North Atlantic Ocean. *Terrestrial, Atmospheric and Oceanic Sciences*, *21*(1), 211–228. https://doi.org/10.3319/tao.2009.04.16.01(iwnop)

Miles, T., Seroka, G., & Glenn, S. (2017). Coastal ocean circulation during Hurricane Sandy. *Journal of Geophysical Research: Oceans*, *122*(9), 7095–7114. https://doi.org/10.1002/2017JC013031

NDBC (2009). *Handbook of automated data quality control checks and procedures*. NOAA Rep. (p. 78). Retrieved from https://www.ndbc.noaa.gov/qc.shtml

Riemer, M., Montgomery, M. T., & Nicholls, M. E. (2010). A new paradigm for intensity modification of tropical cyclones: Thermodynamic impact of vertical wind shear on the inflow layer. *Atmospheric Chemistry and Physics*, *10*(7), 3163–3188. https://doi.org/10.5194/acp-10-3163-2010

Rudzin, J. E., Chen, S., Sanabia, E. R., & Jayne, S. R. (2020). The air-sea response during Hurricane Irma's (2017) rapid intensification over the Amazon-Orinoco River plume as measured by atmospheric and oceanic observations. *Journal of Geophysical Research: Atmospheres*, *125*(18), e2019JD032368. https://doi.org/10.1029/2019jd032368

Seroka, G., Miles, T., Xu, Y., Kohut, J., Schofield, O., & Glenn, S. (2016). Hurricane Irene sensitivity to stratified coastal ocean cooling. *Monthly Weather Review*, *144*(9), 3507–3530. https://doi.org/10.1175/MWR-D-15-0452.1

Shen, J. Q., Qiu, Y., Zhang, S. W., & Kuang, F. F. (2017). Observation of tropical cyclone-induced shallow water currents in Taiwan Strait. *Journal of Geophysical Research-Oceans*, *122*(6), 5005–5021. https://doi.org/10.1002/2017jc012737

Shen, J. Q., Zhang, S. W., Zhang, J. P., Zeng, M. Z., & Fang, W. D. (2021). Observation of continental shelf wave propagating along the eastern Taiwan Strait during Typhoon Meranti 2016. *Journal of Oceanology and Limnology*, *39*(1), 45–55. https://doi.org/10.1007/s00343-020-9346-8

Sreenivas, P., & Gnanaseelan, C. (2014). Impact of oceanic processes on the life cycle of severe cyclonic storm "Jal". *IEEE Geoscience and Remote Sensing Letters*, *11*(2), 519–523. https://doi.org/10.1109/lgrs.2013.2271512

Sun, M., Duan, Y., Zhu, J., Wu, H., Zhang, J., & Huang, W. (2014). Simulation of Typhoon Muifa using a mesoscale coupled atmosphere-ocean model. *Acta Oceanologica Sinica*, *33*(11), 123–133. https://doi.org/10.1007/s13131-014-0561-z

Tang, B., & Emanuel, K. (2010). Midlevel ventilation's constraint on tropical cyclone intensity. *Journal of the Atmospheric Sciences*, *67*(6), 1817–1830. https://doi.org/10.1175/2010jas3318.1

Tang, B., & Emanuel, K. (2012). Sensitivity of tropical cyclone intensity to ventilation in an axisymmetric model. *Journal of the Atmospheric Sciences*, *69*(8), 2394–2413. https://doi.org/10.1175/jas-d-11-0232.1

Vigh, J. L., & Schubert, W. H. (2009). Rapid development of the tropical cyclone warm core. *Journal of the Atmospheric Sciences*, *66*(11), 3335–3350. https://doi.org/10.1175/2009jas3092.1

Wadler, J. B., Zhang, J. A., Rogers, R. F., Jaimes, B., & Shay, L. K. (2021). The rapid intensification of Hurricane Michael (2018): Storm structure and the relationship to environmental and air-sea interactions. *Monthly Weather Review*, *149*(1), 245–267. https://doi.org/10.1175/mwr-d-20-0145.1

Walker, N. D., Leben, R. R., Pilley, C. T., Shannon, M., Herndon, D. C., Pun, I. F., et al. (2014). Slow translation speed causes rapid collapse of northeast Pacific Hurricane Kenneth over cold core eddy. *Geophysical Research Letters*, *41*(21), 7595–7601. https://doi.org/10.1002/2014gl061584

Wang, Y. Q., Rao, Y. J., Tan, Z. M., & Schonemann, D. (2015). A statistical analysis of the effects of vertical wind shear on tropical cyclone intensity change over the western North Pacific. *Monthly Weather Review*, *143*(9), 3434–3453. https://doi.org/10.1175/mwr-d-15-0049.1

Wang, Y. Q., & Xu, J. (2010). Energy production, frictional dissipation, and maximum intensity of a numerically simulated tropical cyclone. *Journal of the Atmospheric Sciences*, *67*(1), 97–116. https://doi.org/10.1175/2009jas3143.1

Winant, C., Mettlach, T., & Larson, S. (1994). Comparison of buoy-mounted 75-kHz acoustic Doppler current profilers with vector-measuring current meters. *Journal of Atmospheric and Oceanic Technology*, *11*(5), 1317–1333. https://doi.org/10.1175/1520-0426(1994)011<1317:cobmka>2.0.co;2

Wong, M. L. M., & Chan, J. C. L. (2004). Tropical cyclone intensity in vertical wind shear. *Journal of the Atmospheric Sciences*, *61*(15), 1859–1876. https://doi.org/10.1175/1520-0469(2004)061<1859:tciivw>2.0.co;2

Yablonsky, R. M., Ginis, I., Thomas, B., Tallapragada, V., Sheinin, D., & Bernardet, L. (2015). Description and analysis of the ocean component of NOAA's operational Hurricane Weather Research and Forecasting Model (HWRF). *Journal of Atmospheric and Oceanic Technology*, *32*(1), 144–163. https://doi.org/10.1175/jtech-d-14-00063.1

Zhang, H., He, H. L., Zhang, W. Z., & Tian, D. (2021). Upper ocean response to tropical cyclones: A review. *Geoscience Letters*, *8*(1), 1–12. https://doi.org/10.1186/s40562-020-00170-8

Zhang, J. A., Cione, J. J., Kalina, E. A., Uhlhorn, E. W., Hock, T., & Smith, J. A. (2017). Observations of infrared sea surface temperature and air-sea interaction in Hurricane Edouard (2014) using GPS dropsondes. *Journal of Atmospheric and Oceanic Technology*, *34*(6), 1333–1349. https://doi.org/10.1175/jtech-d-16-0211.1

Zhang, J. A., Kalina, E. A., Biswas, M. K., Rogers, R. F., Zhu, P., & Marks, F. D. (2020). A review and evaluation of planetary boundary layer parameterizations in hurricane weather research and forecasting model using idealized simulations and observations. *Atmosphere*, *11*(10), 1091. https://doi.org/10.3390/atmos11101091

Zhang, X., Gopalakrishnan, S. G., Trahan, S., Quirino, T. S., Liu, Q., Zhang, Z., et al. (2016). Representing multiple scales in the Hurricane Weather Research and Forecasting Modeling System: Design of multiple sets of movable multilevel nesting and the basin-scale HWRF forecast application. *Weather and Forecasting*, *31*(6), 2019–2034. https://doi.org/10.1175/WAF-D-16-0087.1

Zhang, Z., Wang, Y. Q., Zhang, W. M., & Xu, J. (2019). Coastal ocean response and its feedback to Typhoon Hato (2017) over the South China Sea: A numerical study. *Journal of Geophysical Research: Atmospheres*, *124*(24), 13731–13749. https://doi.org/10.1029/2019jd031377

Zhang, Z., Zhang, W. M., Zhao, W. J., & Zhao, C. W. (2020). Radial Distributions of Sea Surface temperature and their Impacts on the Rapid Intensification of Typhoon Hato (2017). *Atmosphere*, *11*(2), 128. https://doi.org/10.3390/atmos11020128

References From the Supporting Information

Kato, S., Xu, K. M., Wong, T., Loeb, N. G., Rose, F. G., Trenberth, K. E., & Thorsen, T. J. (2016). Investigation of the residual in column-integrated atmospheric energy balance using cloud objects. *Journal of Climate*, *29*(20), 7435–7452. https://doi.org/10.1175/jcli-d-15-0782.1

Trenberth, K. E. (1997). Using atmospheric budgets as a constraint on surface fluxes. *Journal of Climate*, *10*(11), 2796–2809. https://doi.org/10.1175/1520-0442(1997)010<2796:uabaac>2.0.co;2

Coastal downwelling intensifies landfalling hurricanes

Supporting Information

Lewis J. Gramer[1,2,*], Jun A. Zhang[1,2], Ghassan Alaka[2], Andrew Hazelton[1,2], Sundararaman Gopalakrishnan[2]

[1] - Cooperative Institute for Marine and Atmospheric Studies, Miami, FL 33149.
[2] - NOAA Atlantic Oceanographic and Meteorological Lab, Miami, FL 33149.

[*] - Corresponding author: Dr. Lewis J. Gramer, 8930 Caribbean Blvd., Cutler Bay, FL 33157. Email: lew.gramer@noaa.gov. Telephone: +1-305-772-7933. ORCID: https://orcid.org/0000-0003-4772-1991

SUBMITTED: Oct 14, 2021
REVISIONS SUBMITTED: Feb 8, 2022
SECOND REVISIONS SUBMITTED: Apr 8, 2022

Supporting Information

Additional Details on Methods

The model in these case studies was the quasi-operational Basin-scale HWRF (HWRF-B; Zhang et al. 2016; Alaka et al. 2017, 2019, 2020) developed under HFIP. This model uses a single fixed outer domain, with two TC-following nested domains for each TC of interest. The outermost domain covers approximately a quarter of the globe (from 150°E to 30°E longitude and 35°S to 80°N latitude) and has a horizontal grid spacing of 13.5 km. Two telescopic, storm-following nests are centered on each TC: the outer nest (domain D02) covers 16.5° by 16.5° with horizontal grid spacing of 4.5 km and the inner nest (domain D03) covers 5.5° by 5.5° with horizontal grid spacing of 1.5 km. Up to five sets of nested domains can be deployed for a given initialization time to produce high-resolution forecasts for multiple TCs in the North Atlantic and eastern North Pacific.

With the exceptions noted above, HWRF-B and HWRF are identical in configuration, using the Non-hydrostatic Mesoscale Model (NMM) dynamical core operating on a rotated latitude-longitude Arakawa E-grid. The model has 75 hybrid pressure-sigma vertical levels and a model top of 10 hPa. The 2020 version of HWRF-B used for this study was configured with the Ferrier-Aligo microphysics scheme and the Scale-Aware Simplified Arakawa-Schubert (SASAS) cumulus parameterization scheme. The land-surface model is the Noah LSM and the planetary-boundary layer parameterization is the non-local Hybrid Eddy-Diffusivity Mass-Flux (Hybrid EDMF) scheme. The atmospheric radiation parameterizations are the RRTMG shortwave and longwave radiation schemes.

In all nested domains, a vortex initialization procedure is applied to generate a more realistic TC vortex structure. Depending on the intensity of the TC and the existence of a previous forecast, HWRF-B vortex initialization replaces the initial vortex with one of the following vortices, after correcting for intensity and structure: the previous 6-h HWRF-B forecast, a bogus vortex based on an composite of historical TCs, or the original vortex. Furthermore, the initial vortex is improved by assimilating satellite, airborne, and ground-based observations using a hybrid ensemble-variational system based on gridpoint statistical interpolation (GSI). When airborne tail Doppler radar observations are available for a particular TC, an ensemble of 40 HWRF-B members produces error covariances for use in GSI. Otherwise, HWRF-B GSI uses covariances from an ensemble based on NCEP's Global Forecast System (GFS) that is always available.

HWRF-B is coupled to Message Passing Interface Princeton Ocean Model for Tropical Cyclones (MPIPOM-TC). MPIPOM-TC is based on the three-dimensional, primitive equation ocean model known as the Princeton Ocean Model, and its model description can be found in Yablonsky et al. (2015). The MPIPOM-TC domain for these experiments covers latitudes 5°N to 45°N and longitudes 178°W to 15°W with horizontal resolution 1/12°. Outside of the MPIPOM-TC domain, HWRF-B ingests constant SST from the GFS Analysis. MPIPOM-TC uses terrain-following sigma vertical coordinates ($\boldsymbol{\sigma}$). In the coupled HWRF-B, MPIPOM-TC has 40 full $\boldsymbol{\sigma}$-levels from the sea surface to the seafloor, with higher vertical resolution in the region of the main mixed layer and upper thermocline. The maximum ocean depth for the current configuration is 5500m. The model

has a closed boundary condition at the coastline based on a land-sea mask which is consistent with the atmosphere model. The ocean model is initialized from the NCEP Global Real-Time Ocean Forecast System (RTOFS; Mehra and Rivin 2010). In the ocean initialization step, MPIPOM-TC is run for two model days without atmospheric forcing to spin up currents dynamically consistent with the temperature and salinity initialization fields.

For additional information on all of the coupled model configuration details described above, including additional references, please see Alaka et al. (2020).

Three TC case studies from the 2020 North Atlantic hurricane season were evaluated: Sally, Hanna, and Eta. Each TC experienced intensification while approaching land and interacted with the ocean shelf for a period of one day or more. To elucidate processes leading to intensification, model sea-surface fields were analyzed at forecast hours before and immediately after intensification. Supporting Information Table S1 details forecast initialization times for each case and forecast hours chosen for detailed analysis: the forecast hour immediately following intensification and a forecast hour prior to intensification that was near the peak of both air-sea flux and storm kinetic energy (see below). We evaluated the initialization and dynamical evolution of currents and sea temperatures over the shelf in MPIPOM-TC using quality-controlled buoy observations from the NOAA National Data Buoy Center (NDBC 2009; Winant et al. 1994) for one of the case studies, that for TC Sally.

We examined the relationship of air-sea fluxes to total storm kinetic energy and frictional dissipation using a model energy budget following Trenberth (1997) and Kato et al. (2016). Our Equation S1 is the result of integrating Trenberth's (1997) vertically integrated Eq. 16 over the inner TC domain.

$$\left[\iint\int_0^{p_s} KE\ dp\ dA\right]_{t0}^{tH} + \int_{t0}^{tH}\iint\int_0^{p_s} \nabla_p \cdot \vec{\boldsymbol{U}}\, KE\ dp\ dA\ dt - \left[\iint\int_0^{p_s} (c_pT + Lq + \Phi_s) dp\ dA\right]_{t0}^{tH} - \int_{t0}^{tH}\iint\int_0^{p_s} \nabla_p \cdot \vec{\boldsymbol{U}}(c_pT + Lq + \Phi) dp\ dA\ dt + g\ RHF + g\ (THF_d + THF_s) - FD = 0 \quad (1)$$

Eq. S1 includes terms for air pressure p, surface air pressure p_s, kinetic energy KE, storm domain area element A, forecast initialization time t_0 and forecast valid time t_H, wind velocity $\boldsymbol{U}^{\rightarrow}$, specific heat capacity of air c_p, air temperature T, latent heat of evaporation L, specific humidity q, geopotential at the surface ϕ_s and throughout the storm ϕ, respectively, gravitational acceleration g, net radiative heat flux RHF, net turbulent air-sea enthalpy flux over deep water THF_d and over the shelf THF_s, and frictional dissipation FD at the surface. Area element A is taken to consist of the region of instantaneous 17.5 ms^{-1} (34 kt) winds within the innermost domain (e.g., Figure 1). Square brackets denote differences between instantaneous values evaluated at different forecast hours.

We follow Emanuel (1986) and Wang and Xu (2010) in considering a simplified version of the above energy budget consisting of only the terms highlighted in red. This simplified equation elucidates the relationship between TC intensity change and TC interaction with the ocean and

allows for the analysis of surface enthalpy fluxes over the shelf as a separate contribution to the budget. This study considers turbulent air-sea enthalpy fluxes only at gridpoints where 10 m winds are 17.5 ms^{-1} or greater. Fluxes within atmospheric grid cells over ocean model topography of 150 m depth or less are summed in the THF_s term; all other air-sea enthalpy fluxes are accumulated in THF_d. Frictional dissipation (*FD*) is estimated from predicted 10 m wind speeds as per Kato et al. (2016). We calculate total kinetic energy averaged over all vertical levels in the inner atmospheric model domain. All other terms in Eq. S1 (terms in black) are treated as residuals.

Additional Figures

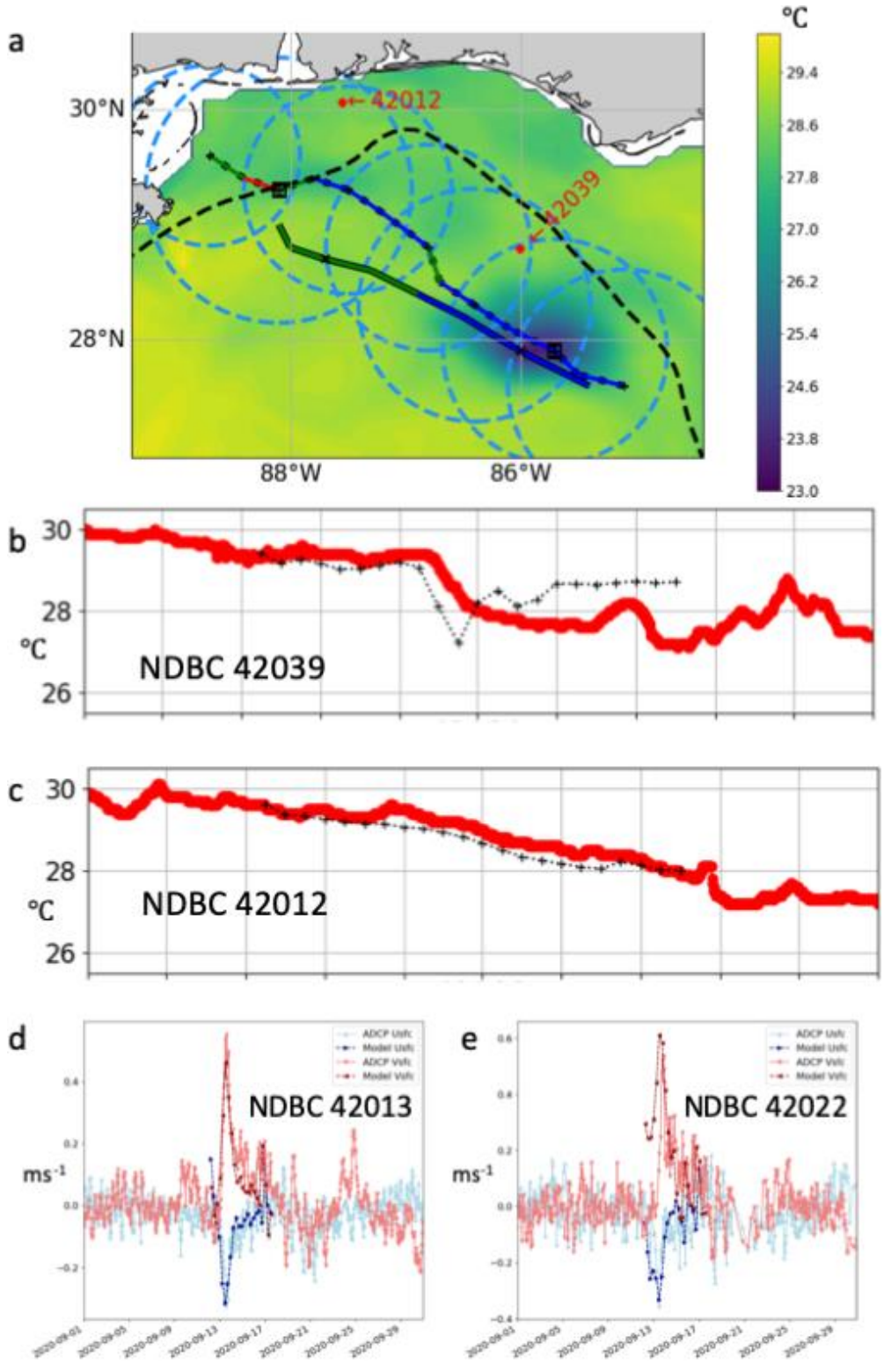

Figure S1: Data from NOAA NDBC buoys in the Gulf of Mexico for 10-20 Sep 2020: (a) map showing model SST [ºC] for forecast hour 54, together with location of buoys (red dots) along Sally's HWRF-B forecast track (dashed outline, colored by storm intensity) and 17.5 ms^{-1} wind radii (circles). Best track is also outlined with solid black. Model 150 m isobath is a dashed black line. (b) Near-surface sea temperature (ºC; red) compared with model SST (dotted black "+") for buoy 42039 in the deeper Gulf, water depth 281 m. (c) Near-surface temperature and model SST for buoy 42012 on the northern Gulf shelf in 24 m of water. (d) Near-surface currents [m/s] west-to-east across-shore (u, blue) and south-to-north alongshore (v, red); solid lines show quality-controlled ADCP measurements (top good bin) from two buoys on west Florida shelf, dashed lines show ocean model output (topmost model level).

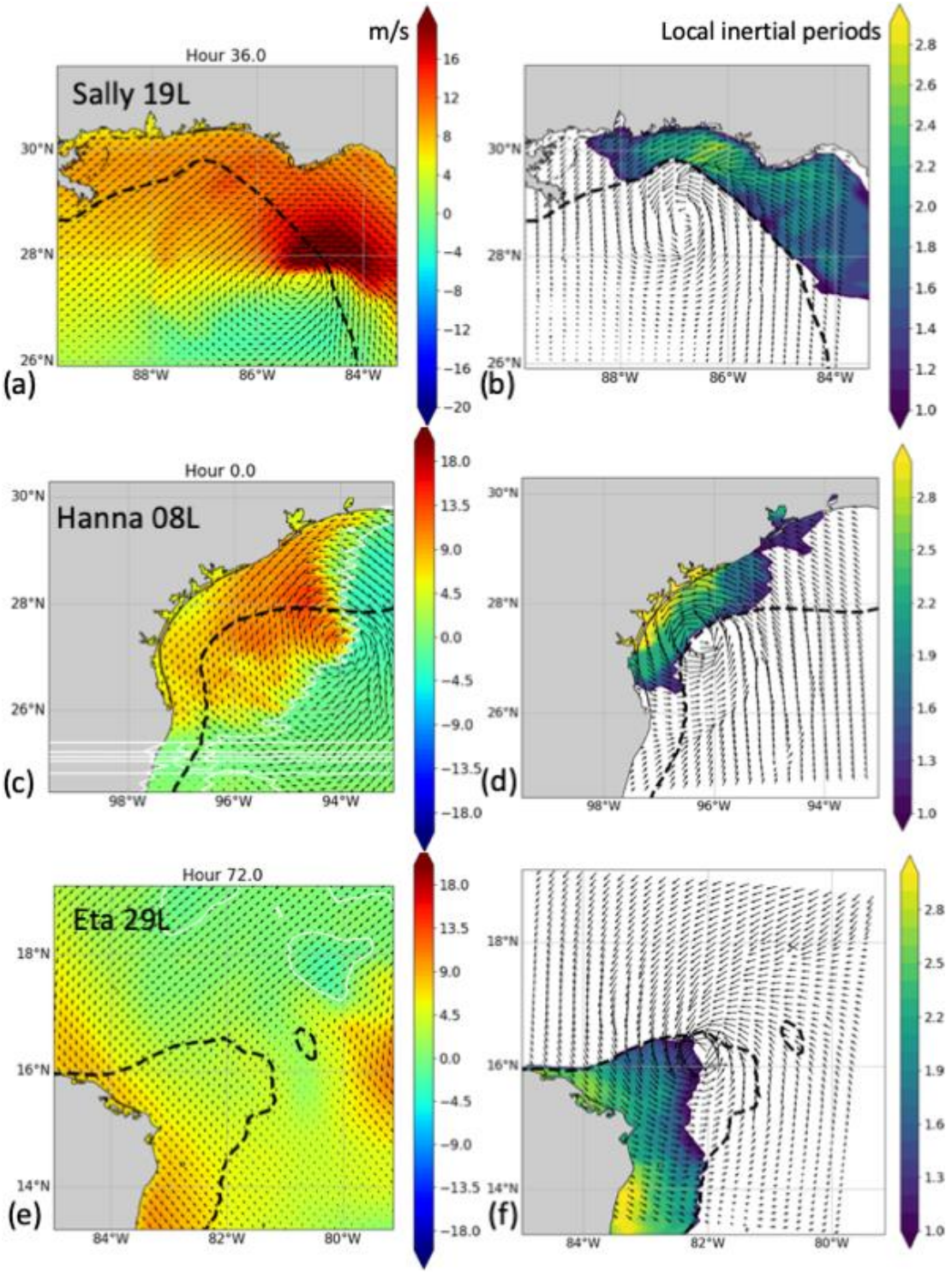

Figure S2: (a,c,e) Snapshot of wind vectors and magnitude of downwelling-favorable wind component (alongshore ms^{-1}; shading, with zero contour marked in white) at a forecast hour one inertial period prior to intensification; (b,d,f) Wind vectors at hour just prior to intensification, and accumulated number of inertial periods (multiples of 22 h at the latitude of Sally and Hanna, 42 h for Eta; shading) during which downwelling-favorable winds were blowing over the shelf. Thick dashed black line shows the 150 m isobath outlining the shelf regions; land is in gray.

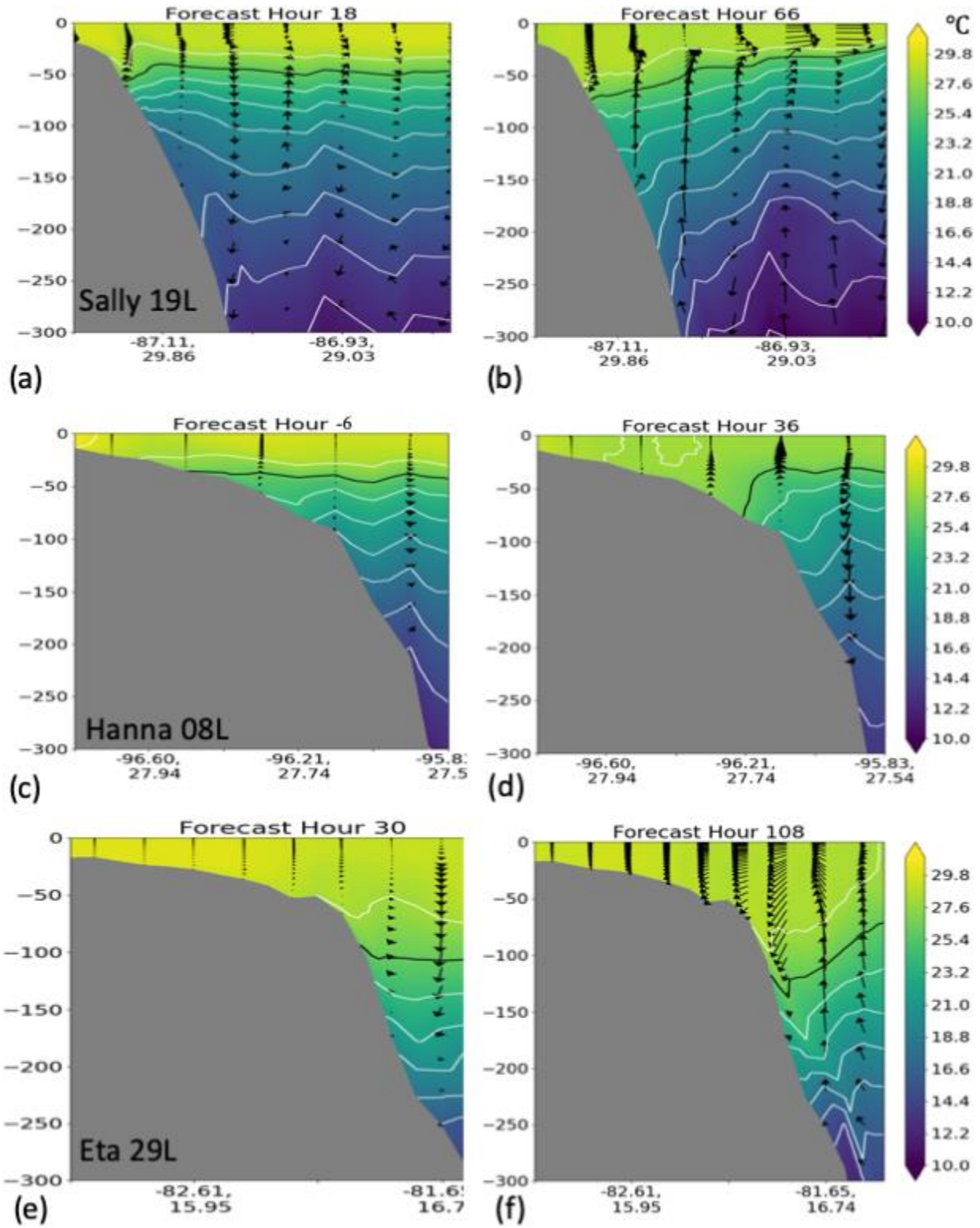

Figure S3: Section plots (along the same section lines shown in Figure 2, middle panel), shown here at two other times separated from each other by two local inertial periods. These show the evolution of the downwelling circulation cell (currents in black arrows) and depression of isotherms (sea temperature in ºC) over the shelf that formed ahead of the passage of each TC.

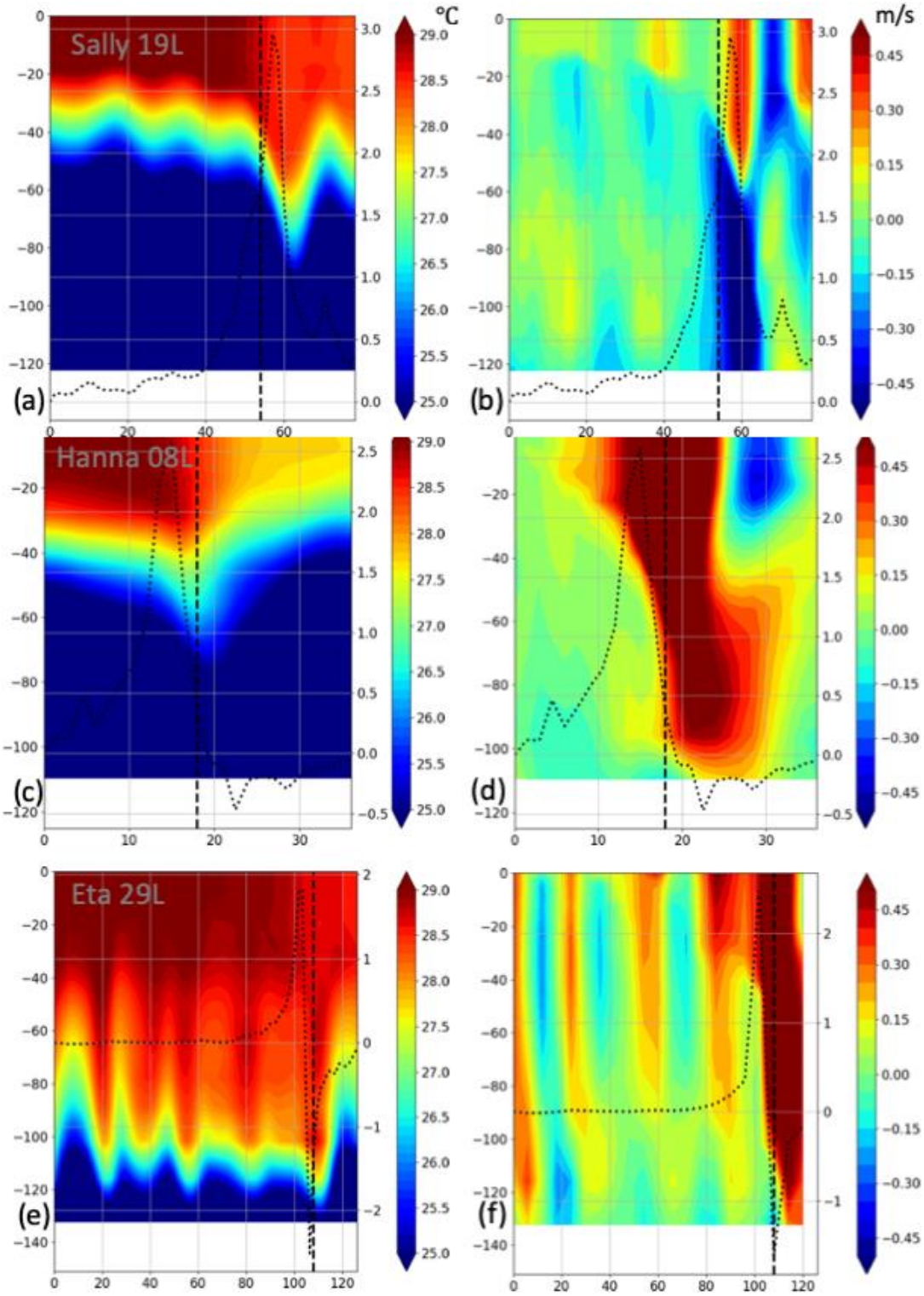

Figure S4: Hovmöller diagrams showing change in vertical ocean profiles at a point near the 150 m isobath along each of the onshore tracks in the left and middle panels of Figure 2. (a,c,e) Ocean temperature [ºC] and (b,d,f) cross-shelf currents [m/s]. The right axis and black dotted line show along-shore 10 m wind stress from the model [N/m^2]. Dashed vertical black line shows the forecast hour highlighted in Figure 2 and in the left panels of Figures 1, 3, and 4.

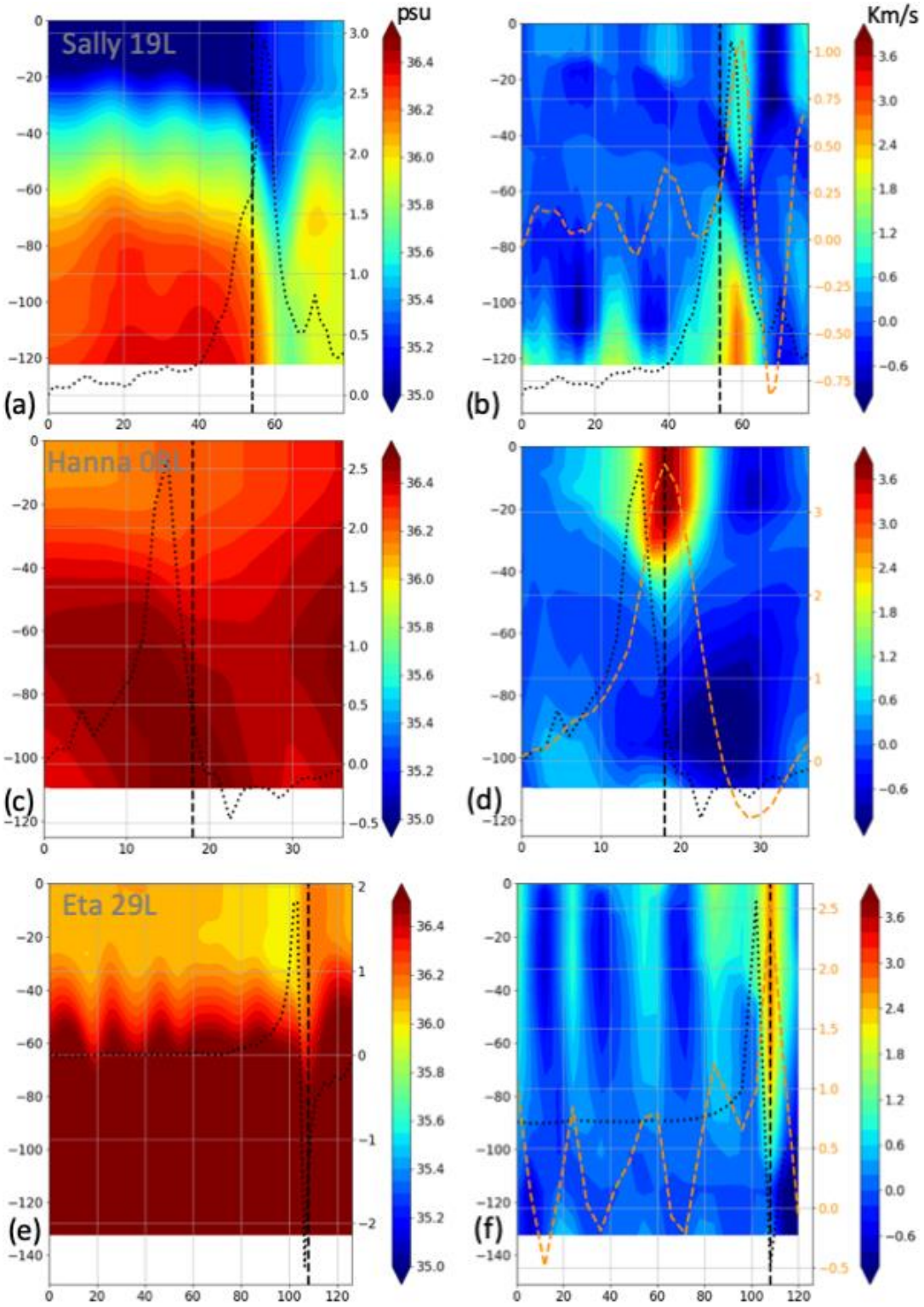

Figure S5: Hovmöller diagrams similar to those in Figure S4, showing changes in: (a,c,e) salinity [psu] and (b,d,f) cross-shore heat transports [K·m/s]. For left-hand panels, right axis and black dotted line show alongshore 10 m wind stress from the model [N/m^2]. For right-hand panels, black dotted line still shows along-shore wind stress but with no corresponding axis, while the dashed orange line and right axis show cross-shore net heat flux [MW/m^2] relative to 26 °C.

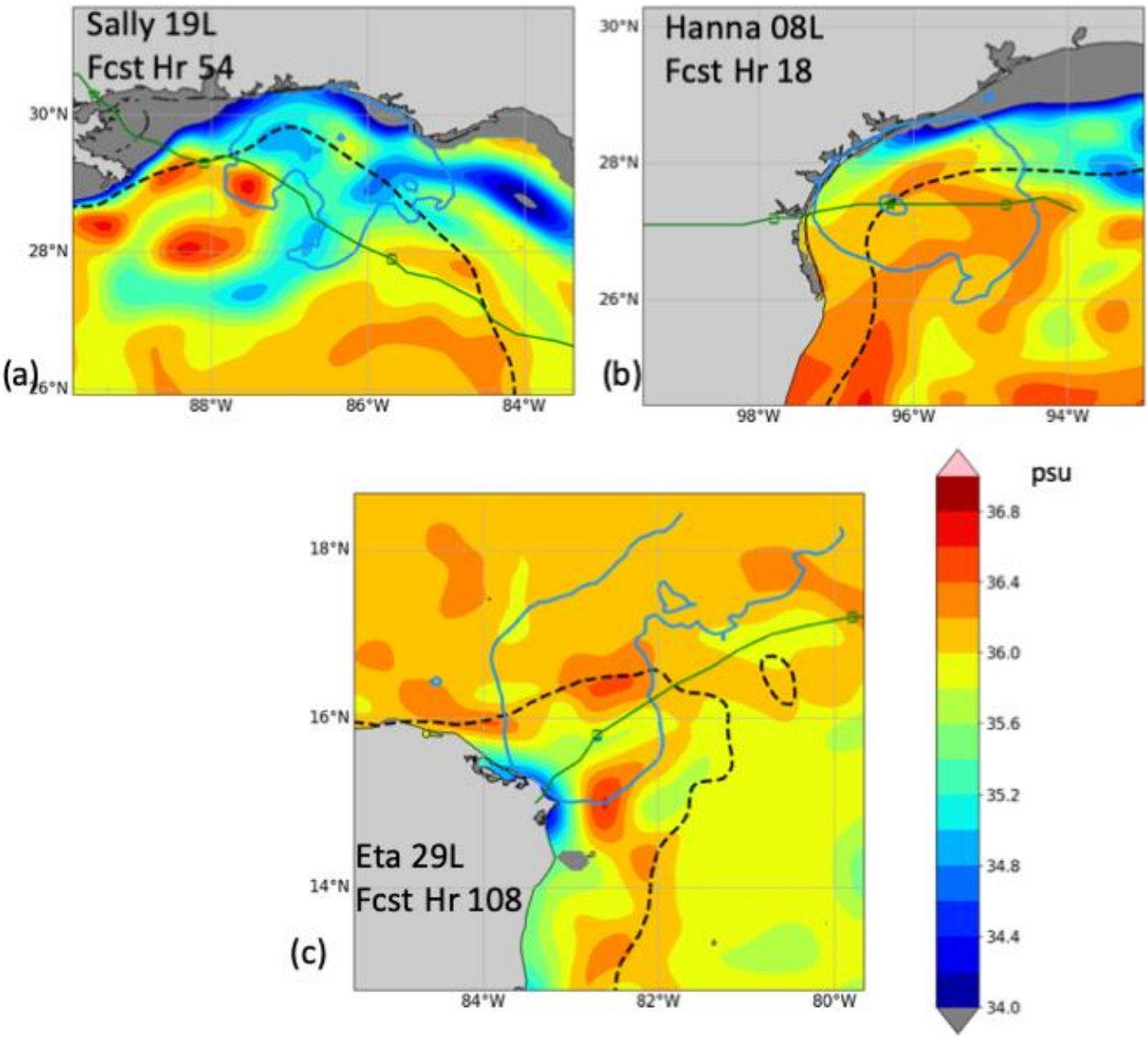

Figure S6: Model sea-surface salinity (psu; shading) at forecast hour just prior to intensification for each of the three case studies. Contour of winds > 17.5 m/s (blue) and the 150 m isobath (black dashed), and forecast TC track and positions (green lines and squares) as in Figures 1-3.

Table S1: Storm forecast initialization time, forecast hours (chosen before and after intensification) that are highlighted in Figs.1-4, peak intensity change in the 24 h following the first highlighted forecast hour, and environmental characteristics during the highlighted period: environmental deep vertical wind shear (200-850 mbar), translation speed of the storm, total air-sea enthalpy flux (THF), and percentage of THF deriving from shelf waters.

Storm	**Forecast Init. Time**	**Fcst. Hours Highlighted**	**Forecast Intensity Change in 24 h; ms^{-1}**	**Environ. Shear; ms^{-1}; Direction**	**Fcst. Storm Transl. Speed; ms^{-1}; Dir.**	**Total Air-Sea Heat Flux (THF); TJ**	**% THF from shelf**
Sally 19L	0600Z 12 September 2020	54, 66	+26	13 WSW	3.0 SE	$1.0x10^7$	60%
Hanna 08L	1800Z 24 July 2020	18, 24	+18	5.1 NW	4.1 E	$3.5x10^6$	80%
Eta 29L	0600Z 30 October 2020	108, 114	+11	8.7 S	3.6 NE	$1.8x10^7$	40%